Biomaterials Science

PAPER

View Article Online
View Journal | View Issue

Cite this: *Biomater. Sci.*, 2020, **8**, 712

Methotrexate–Mn^{2+} based nanoscale coordination polymers as a theranostic nanoplatform for MRI guided chemotherapy†

Yan Wu,[a] Li Xu,[b] Jiwen Qian,[b] Leilei Shi,[b] Yue Su, [b] Youfu Wang, *[b] Dawei Li*[a] and Xinyuan Zhu *[b]

Theranostic nanoplatforms based on magnetic resonance imaging (MRI) technology have drawn much attention due to their inherent advantages such as non-invasiveness and high spatial resolution, but their construction is usually complicated and the compositions are uncontrollable. Herein, a simple and controllable theranostic nanoplatform by replacing a chelating agent with a chemotherapeutic drug directly was proposed. In detail, we elaborately synthesized Mn^{2+} and methotrexate (MTX) based nanoscale coordination polymers (NCPs) coated with poly(ethylene glycol) (PEG), MTX-Mn@PEG, in which Mn^{2+} ions served as MRI contrast agents (CAs), MTX was used as a chemotherapy drug and PEG provided a stable environment for nanoparticles, respectively. The obtained MTX-Mn@PEG NCPs showed a relatively uniform size, a pH-responsive feature and long blood circulation to enrich in the tumor location through the enhanced permeability and retention (EPR) effect. We determined the composition and coordination mechanism of MTX-Mn@PEG through thermogravimetric analysis (TGA), Fourier transform infrared (FI-TR) spectroscopy, powder X-ray diffraction (XRD) and so on. We determined the composition and coordination mechanism of MTX-Mn@PEG with the molar ratio of MTX to Mn^{2+} as 1 : 1. Then we confirmed that the antitumor ability was mediated by MTX through MTT and cell apoptosis assay *in vitro*. *In vivo* MR imaging and antitumor assays demonstrated the excellent effect of the NCPs in diagnosis and therapy of tumors. Overall, these novel MTX-Mn@PEG NCPs provide a theranostic nanoplatform for cancer treatment.

Received 30th September 2019,
Accepted 10th November 2019

DOI: 10.1039/c9bm01584a

rsc.li/biomaterials-science

1. Introduction

Recently, malignant tumors have become one of the main diseases threatening human lives worldwide.[1,2] Although tumor biology has made great progress in the past two decades, this situation has not improved significantly.[3] Fortunately, the rapid development of theranostic systems which integrate the diagnosis and therapy of tumors into one nanoplatform has brought a new dawn to the treatment of tumors.[4–6] Among these theranostic methods, the nanoplatforms based on MRI technology have drawn much attention from researchers because of their inherent advantages such as non-invasiveness and high spatial resolution.[7–9] However, the MRI-based theranostic nanoplatforms have a fatal shortcoming: the CAs such as Gd^{3+} and Mn^{2+} are harmful to the human body.[10,11] To resolve this problem, chelating agents such as diethylenetriaminepentaacetic acid (DTPA) or porphyrin must be used to block the toxicity of CAs during usage for the sake of reducing their harm to the human body.[12–14] Unfortunately, the application of chelating agents will increase the synthesis steps and price of the nanoplatforms resulting in complicated compositions and high cost of the nanoplatforms, and also bring side effects to the human body by themselves.[15,16]

Based on the abovementioned analysis, we envisage whether the chelating agents used in MRI technology can be replaced with chemotherapeutic drugs directly so as to form NCPs to eliminate the influence of chelating agents. NCPs are new theranostic nanoplatforms containing the merits of both organic nanoparticles and inorganic nanoparticles.[17,18] They have merits including simple composition and easy fabrication, and have attracted more and more interest recently.[19–22] Methotrexate (MTX), a widely used antitumor chemodrug in the clinic,[23,24] can be used to replace the chelating agents because both the polycarboxylic groups and nitrogen heterocycle in MTX can coordinate with metal ions to stabilize the

[a]*School of Pharmacy, Shanghai Jiao Tong University, 800 Dongchuan Road, Shanghai 200240, PR China. E-mail: daweili@sjtu.edu.cn*
[b]*School of Chemistry and Chemical Engineering, Shanghai Jiao Tong University, 800 Dongchuan Road, Shanghai 200240, PR China. E-mail: wyfown@sjtu.edu.cn, xyzhu@sjtu.edu.cn*

†Electronic supplementary information (ESI) available: DLS at different times, zeta-potential, EDS and ICP-MS results of MTX and MTX-Mn@PEG and images of mice. See DOI: 10.1039/c9bm01584a

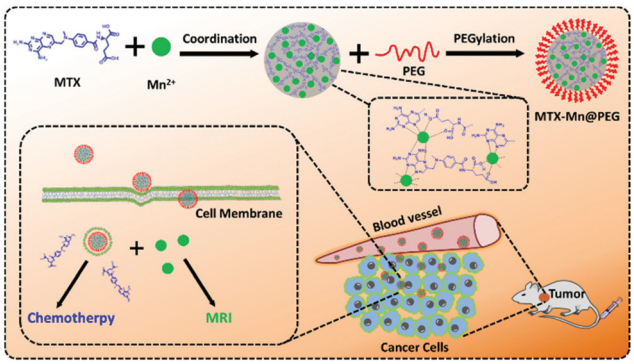

Scheme 1 Schematic illustration of the composition of MTX-Mn@PEG NCPs and their use as a theranostic nanoplatform for MRI guided chemotherapy *in vivo*.

CAs for MRI. Thus, the replacement of the chelating agent with the MTX drug can not only reduce the steps of synthesizing the theranostic nanoplatform, but also eliminate side effects of the chelating agent on the human body. Additionally, the chemotherapeutic drug coordination with metal ions to form NCPs directly instead of being fed by physical adsorption can increase the proportion of chemotherapeutic drugs in the nanoplatforms greatly and make it controllable.

In this work, we successfully fabricated the MTX-Mn@PEG based NCPs as a theranostic nanoplatform for MRI guided chemotherapy as shown in Scheme 1. As difunctional NCPs, MTX-Mn@PEG contains MTX as the chemical drug and manganese ions with excellent ability in MRI.[25,26] The surfaces of MTX-Mn nanoparticles are coated with PEG by hydrophobic interactions for long circulation in blood to achieve the EPR effect.[27–29] We confirmed the compositions and possible coordination mechanism of MTX-Mn@PEG by methods of transmission electron microscopy (TEM), TGA, FI-TR, XRD and so on. Then we investigated whether the antitumor ability of MTX-Mn@PEG was mediated by MTX through MTT and cell apoptosis assays *in vitro*. Finally, we verified that the antitumor effect of MTX-Mn@PEG was better than that of MTX *in vivo*. Meanwhile, we achieved high resolution MR imaging in the tumor location of mice which can be a guide for cancer therapy. Overall, the MTX-Mn@PEG NPCs are a very promising theranostic nanoplatform for cancer treatment.

2. Experimental section

2.1 Materials

All materials were commercially available and used as received without further purification. MTX and indocyanine green (ICG) were offered by Aladdin Co. Ltd (Shanghai, China). *N*,*N*-Dimethylformamide (DMF), $MnCl_2$ and triethylamine (TEA) were supplied by Sinopharm Chemical Reagent co. Ltd (Shanghai, China). 1,2-Distearoylsn-*glycero*-3-phosphoethanolamine-*N*-[methoxy(polyethylene glycol)$_{2k}$] (DSPE-PEG$_{2K}$) was supplied by 9i Technology Co., Ltd (Shanghai, China). Deionized water was obtained from a Milli-Q Plus gradient system. HeLa cells, a cervical cancer cell line of human, were purchased from the American Type Culture Collection. The cell culture medium, Dulbecco's modified Eagle's medium (DMEM), was supplied by Gibco BRL (Grand Island, USA). Fetal bovine serum (FBS) was afforded by the same company as DMEM. A dead cell apoptosis kit was obtained from Thermo Fisher Scientific Co. Ltd (Shanghai, China).

2.2 Synthesis of MTX-Mn@PEG

The synthesis procedure of MTX-Mn@PEG was similar to those in previous reports.[19,20,30] Briefly, methanol (10 mL) containing MTX (200 mg) and TEA (0.2 mL) and DMF (10 mL) containing $MnCl_2$ (40 mg) were mixed under sonication until yellow turbidity appeared. DSPE-PEG$_{2K}$ (200 mg) was added into the MTX-Mn suspension followed by vigorous stirring at 65 °C for 22 h, then the mixed solution was centrifuged using Centrifuge 5424 R (Eppendorf, Germany) at 7000 rpm for 8 min and the precipitate was washed with deionized water three times. The finally obtained precipitate, denoted as MTX-Mn@PEG, was dispersed in deionized water for further use.

2.3 Characterization of MTX-Mn@PEG

The morphology of MTX-Mn@PEG was observed using a 120 kV TEM (Tecnai G2 Spirit Biotwin). Dynamic light scattering (DLS) was performed to test the hydrodynamic size of MTX-Mn@PEG. Zeta potentials of MTX-Mn and MTX-Mn@PEG were measured to find the surface charge of the nanoparticles. DLS and Zeta potentials were performed with a Size and Zeta Potential Analyzer (Malvern, UK).

2.4 Compositions of MTX-Mn@PEG

To determine the percentage of MTX in MTX-Mn@PEG, the standard absorption curve of MTX at 302 nm was obtained under ultraviolet-visible (UV-vis) spectroscopy. 1 mg synthesized MTX-Mn@PEG was added into 1.25 mL deionized water and shaken to be dissolved totally, and then 0.8 mg of EDTA was added to free the MTX from the NCPs. Later, the solution was diluted 20 times with deionized water to obtain an appropriate absorbance value. Then the mixture was examined at a 302 nm wavelength. The percentage of MTX was calculated using eqn (1).

$$\text{MTX}\ (\%) = (\text{weight of [MTX]})/(\text{weight of [MTX-Mn@PEG]}) \times 100\% \quad (1)$$

The percentage of the Mn element was confirmed by inductively coupled plasma–mass spectroscopy (ICP-MS), energy dispersive spectroscopy (EDS, FEI Talos F200X, USA) and TGA. The percentage of PEG was calculated using eqn (2).

$$\text{PEG}\ (\%) = (1 - \text{Mn}\ \% - \text{MTX}\ \%) \times 100\% \quad (2)$$

2.5 Coordination mechanism of MTX-Mn

To investigate the coordination mechanism of MTX-Mn@PEG, MTX-Mn nanoparticles were synthesized to eliminate the influence of PEG. Next, XRD was used to verify whether it formed

crystals or not. 500 mg dry MTX-Mn nanoparticles were measured by XRD (Advance Da Vinci, Germany) over the range 3–90° (2θ) at 40 kV and 15 mA. Later, 3 mg MTX and 3 mg MTX-Mn were measured with a differential scanning calorimeter (DSC, PerkinElmer DSC8500, USA) from 20 °C to 220 °C at a speed of 10 °C min^{-1}. Then, the UV-vis spectrum was utilized to investigate whether the stretching vibrations of chemical groups in MTX were influenced by Mn^{2+} or not. MTX (0.1 mg), MTX-Mn (0.12 mg) and $MnCl_2$ (0.01 mg) were dissolved in 1 mL methanol, respectively, and were scanned with a UV-vis spectrometer (Thermo Scientific, USA) from 200 to 500 nm using a quartz tube. FT-IR was also applied for the structural analysis. 2 mg MTX and MTX-Mn were mixed with 200 mg KBr and pressed into pellets, respectively. Then, the pellets were scanned with an FT-IR spectrometer (Nicolet, USA).

2.6 *In vitro* release studies

1 mg MTX-Mn@PEG was added into deionized water (3 mL) and shaken to dissolve totally. Then the MTX-Mn@PEG solution was placed into a dialysis bag whose molecular weight cut off (MWCO) was 1 kDa. The dialysis bags were immersed in tubes containing 30 mL PBS with a pH of 5.5 or 7.4, and then the tubes were shaken in a blender at 120 rpm at 37 °C. At predetermined time points, 3 mL PBS was withdrawn and 3 mL fresh PBS was added into the tubes respectively. The amount of MTX released over time was measured from the UV-vis absorbance at 302 nm and then calculated with the standard curve previously mentioned.

2.7 *In vitro* T_1-weighted MR imaging

Different concentrations of $MnCl_2$ and MTX-Mn@PEG in deionized water (the concentration of Mn^{2+} is the same for each control group) were used and tested on a 0.5 T low field MR scanner at room temperature. The corresponding longitudinal relaxivity (r_1) values of $MnCl_2$ and MTX-Mn@PEG were inferred from the standard curve plotted with concentrations of Mn^{2+} and the values of corresponding $1/T_1$ relaxation time (s^{-1}).

2.8 *In vitro* cell experiments

HeLa cells were cultured with full DMEM with 10% FBS and 1% antibiotics. The atmosphere for cell culture was moist containing 5% CO_2 and maintained at 37 °C.

2.8.1 *In vitro* cytotoxicity evaluation. To examine the inhibition ability of MTX-Mn@PEG on HeLa cells, a standard methyl thiazolyl tetrazolium (MTT) assay was conducted. 100 μL HeLa cells, at a density of 6×10^4 mL^{-1}, were seeded into each well of a 96-well plate. 20 hours later, different concentrations of MTX and MTX-Mn@PEG (concentrations of MTX were the same with free MTX) were added into the wells. 72 hours later, 20 μL MTT (5 mg mL^{-1}) was introduced into every well. 4 hours later, the stale DMEM was discarded carefully, and then 200 μL of dimethyl sulfoxide (DMSO) was placed into each well for 20 minutes to dissolve the crystals of MTT. The absorbance value of each well was examined with a Multiscan Spectrum (BioTek, Synergy2, USA) at a wavelength of 490 nm.

2.8.2 Cell uptake assay. To evaluate the rate of MTX-Mn@PEG taken up by HeLa cells, the cells were seeded into each well of a 12-well plate with a quantity of 2×10^5, and then cultured in the incubator for 20 hours. 0.2 mg mL^{-1} MTX-ICG-Mn@PEG was added at predetermined time points of 0, 0.5, 1, 2, and 4 h. For the fluorescence imaging experiment, the stale DMEM was discarded, and new DMEM containing dyes were supplemented into the plates. The cellular nucleus was stained through incubation with 0.01 mg mL^{-1} (in DMEM) Hoechst 33342 for 25 minutes at 37 °C. Finally, the plates were washed with pre-cooled PBS 3 times, and observed with a fluorescence microscope. For the flow cytometry experiment, the staining procedure was the same without Hoechst 33342 staining. The cells were harvested, washed in PBS by centrifugation at 1000 rpm for 5 minutes, transferred into falcon pipes, and analyzed by flow cytometry (BD FACSCalibur, USA).

2.8.3 Apoptosis analyses by flow cytometry. Cell apoptosis assay was conducted to estimate whether the antitumor ability of MTX-Mn@PEG came from MTX or not. 2×10^5 HeLa cells were seeded into every well of 12-well plates and cultured overnight. MTX (0.2 mg mL^{-1} in full DMEM) co-cultured with HeLa cells served as a comparative group, and MTX-Mn@PEG (0.25 mg mL^{-1}) served as the experimental group. After 72 hours, the cells were resuspended with trypsin, washed 2 times and stained with Dead Cell Apoptosis Kit according to the protocol. Cells cultured normally and stained with fluorescein isothiocyante (FITC) and propidium iodide (PI) were regarded as a control. Finally, all samples were disposed within an hour with a BD LSRFortessa flow cytometer.

2.9 Animals and tumor models

All the 5-week-old BALB/c nude mice (20–22 g) and Sprague–Dawley (SD) rats (200–220 g) were provided by the Chinese Academy of Sciences (Shanghai). All experiments involving animals were conducted according to the procedure ratified by the Institutional Animal Care and Use Committee (IACUC) of Shanghai Jiao Tong University. The xenograft tumor mice were established by subcutaneous inoculation of HeLa cells (2×10^6) at the right armpit per mouse. The mice were randomly divided into four groups (n = 5): PBS, $MnCl_2$, MTX, and MTX-Mn@PEG when the tumors grew to about 100 mm^3. The volume of the tumor was calculated using eqn (3).

$$V\ (\mathrm{mm}^3) = 1/2 \times \text{length (mm)} \times \text{width (mm)} \times \text{width (mm)} \quad (3)$$

2.9.1 *In vivo* MR imaging. When the tumors were grown to 1000–1500 mm^3, BALB/c nude mice bearing HeLa tumors were divided into two groups and intravenously injected with $MnCl_2$ (200 μL, 0.23 mg mL^{-1}) or MTX-Mn@PEG (200 μL, 1 mg mL^{-1}). Then the mice were anesthetized by inhalation of isoflurane. MR imaging was performed on a 0.5 T MR scanner at 0, 1, 4, 8 and 24 h. The conditions of MRI were as follows: the repetition time was 400 ms, the echo time was 18.2 ms, the length of the square field of view was 100 mm and the slide width and gap were 2.5 mm and 1.0 mm, respectively.

2.9.2 *In vivo* pharmacokinetics assay. SD rats were divided into two groups (5 rats per group) by bodyweight stochastically. The rats were administered with MTX and MTX-Mn@PEG in PBS solution *via* tail vein injection. The doses of both groups were 1 mL and the concentration of MTX was 1 mg mL^{-1}. At a predetermined time, 500 μL blood was obtained from the mice. All the blood samples were separated by centrifugation at 13 000 rpm for 25 minutes at 4 °C. The upper light yellow suspension was moved to new tubes and the amount of MTX was measured by high performance liquid chromatography.

2.9.3 *In vivo* antitumor efficacy. The mice of 4 groups were treated with 0.2 mL PBS (control), MTX (9.6 mg kg^{-1}), $MnCl_2$ (2.7 mg kg^{-1}), and MTX-Mn@PEG (12 mg kg^{-1}) respectively, *via i.v.* injection every 2 or 3 days. Simultaneously, the changes of body weights were measured with an electronic weighing scale and the volume of tumors was recorded with an electronic Vernier Caliper, respectively. After 14 days, all the mice were sacrificed and the tumors were taken out for weighing and photographing.

2.9.4 Hematoxylin–eosin (H&E) and TUNEL assay. For histological examinations, at the end of treatments, all the mice were sacrificed by dislocating their cervical vertebra to death. Next, all the major organs (lung, liver, spleen, kidney and heart) and tumors were extracted from the bodies and immersed in paraformaldehyde (4%, w/v). All the organs were treated according to the protocol of H&E assay. The tumors were stained with H&E and subjected to terminal deoxynucleotidyl transferase dUTP nick-end labelling (TUNEL) for evaluation of the antitumor effect of MTX and MTX-Mn@PEG.

2.10 Statistical analysis

All data were presented as the mean ± standard deviation (SD). Student's *t*-test was employed to analyse the data. $P < 0.05$ means statistically significant difference.

3. Results and discussion

3.1 Fabrication and characterization of MTX-Mn@PEG

The fabrication processes of MTX-Mn@PEG are shown in Scheme 1. The MTX-Mn nanoparticles were fabricated through coordination bonds between MTX and Mn^{2+}, and DSPE-PEG_{2K} was coated onto the surface of MTX-Mn nanoparticles *via* hydrophobic interactions. The TEM image (Fig. 1A) shows that the obtained MTX-Mn@PEG NCPs are spherical and uniform in size. The average hydrodynamic diameter of MTX-Mn from DLS was about 81.5 ± 9.7 nm while it changed to about 93.3 ± 10.3 nm after the coating of PEG (Fig. 1B). The average hydrodynamic diameter of MTX-Mn@PEG increased up to 118.9 ± 14.6 nm after 48 h indicating a relatively good stability of PEG on the surface of the nanoparticles (Fig. S1†). The zeta potential of MTX-Mn measured in 50 mM PBS at 25 °C was about −23.7 ± 2.9 mV, while it changed to −15.8 ± 1.3 mV after coating with PEG with the zeta potential of PEG being nearly neutral, further proving that DSPE-PEG_{2K} was coated onto MTX-Mn (Fig. S2†). All the results above indicated that MTX-Mn@PEG NCPs were successfully fabricated.

3.2 Compositions of MTX-Mn@PEG

TEM and energy dispersive spectroscopy (EDS) mapping (Fig. 2A) were conducted to confirm the presence of the manganese element in MTX-Mn@PEG NCPs. The results showed that the manganese element was located with elements C and N from MTX. It is clearly proved that manganese was doped into MTX-Mn@PEG uniformly, and the weight ratio of the manganese element in the particles accounted for 6.79% (Table S1†). As this datum was influenced by the carbon element on the TEM grid, we performed some other experiments to explore the content of the manganese element in the NCPs. ICP-MS results (Table S2†) showed that the weight of manganese in MTX-Mn@PEG is about 12.1%. Additionally, the TGA result showed that the percentage of manganese dioxide was about 17.2% which means 10.7% for the manganese element (Fig. 2B). Therefore, all the results above revealed that the manganese element accounts for about 10% in the NCPs. MTX in the NCPs was found to be about 80% from the characteristic absorbance of MTX at 302 nm and the standard curve of MTX (Fig. 2C). The PEG was found to account for 10% in the NCPs using the equation mentioned above, and this datum can be proved by the TGA result (Fig. 2B) that the weight of MTX-Mn@PEG changed from 100% to 89.3% during

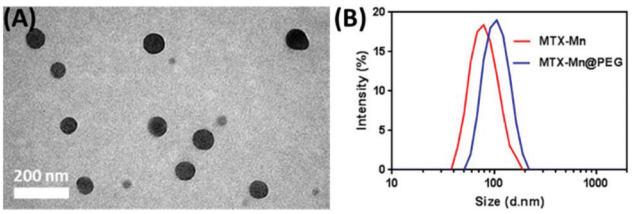

Fig. 1 (A) TEM image of MTX-Mn@PEG with a scale bar of 200 nm. (B) Hydrodynamic diameters of MTX-Mn and MTX-Mn@PEG in water.

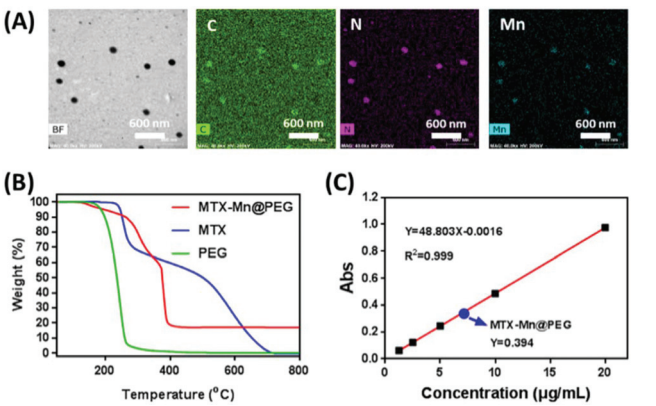

Fig. 2 (A) TEM image and EDS mapping of MTX-Mn@PEG NCPs with a scale bar of 600 nm. (B) TGA curves of MTX, MTX-Mn@PEG and PEG. (C) Standard curve of the characteristic absorbance of MTX at 302 nm at different concentrations.

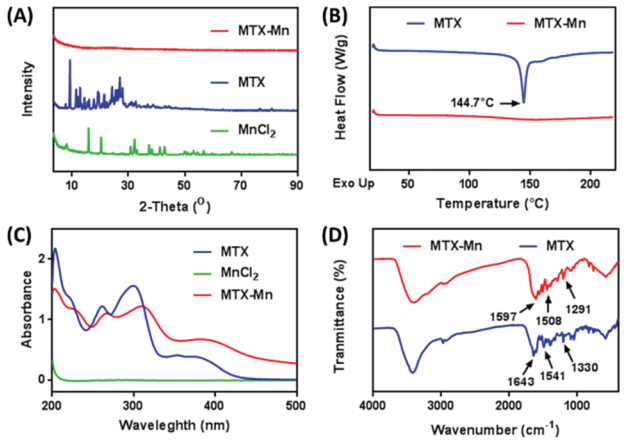

Fig. 3 (A) PXRD patterns of MTX-Mn, MTX, and $MnCl_2$. (B) DSC plots of MTX and MTX-Mn. (C) UV-vis spectra of MTX, $MnCl_2$, and MTX-Mn. (D) FT-IR spectra of MTX and MTX-Mn.

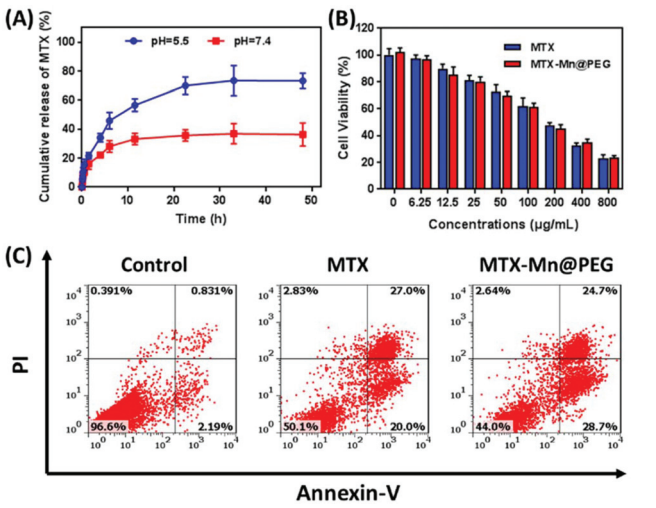

Fig. 4 (A) Drug release profiles of MTX-Mn@PEG in pH = 5.5 and 7.4 PBS solutions. (B) Cell viability of HeLa cells cocultured with MTX and MTX-Mn@PEG at gradient concentrations after 72 h. (C) Cell apoptosis of HeLa cells induced by MTX and MTX-Mn@PEG after incubation for 72 h.

200–300 °C referring to the weight loss of PEG. Finally, the composition of MTX-Mn@PEG NCPs consisted of 80% MTX, 10% Mn and 10% PEG. After calculation, the molar ratio of MTX to Mn in MTX-Mn@PEG NCPs was approximated to 1 : 1.

3.3 Coordination mechanism of MTX-Mn

Fig. 3A reveals that some characteristic peaks of $MnCl_2$ and MTX disappeared after assembling together showing an irregular curve in powder XRD. The DSC of MTX showed an endothermic peak at 144.7 °C referring to the crystal nature that disappeared after coordinating with manganese (Fig. 3B). So the nature of MTX-Mn is amorphous. After coordination with Mn, the characteristic absorption peaks of MTX in UV-vis spectra at 258 nm and 302 nm were red shifted to 269 nm and 313 nm, respectively (Fig. 3C). The red shift of the characteristic absorption peaks of MTX can be attributed to the decrease of electron cloud density after coordination with Mn^{2+}.[31] FT-IR spectral analysis (Fig. 3D) figured out that the peaks at 1643 and 1541 cm^{-1} referring to stretching vibrations of the double bonds of COO^- groups in MTX were shifted to 1597 and 1508 cm^{-1},[32] and the peak at 1330 cm^{-1} assigned to the stretching vibrations of C–N in the nitrogen heterocycle of MTX was shifted to 1291 cm^{-1}.[33] All the results above confirmed that the COO^- groups and nitrogen heterocycle of MTX took part in the coordination. Taking into consideration the molar ratio of MTX to Mn in MTX-Mn@PEG, the coordination mechanism of MTX-Mn@PEG was one Mn^{2+} coordinating with one MTX on average as shown in Scheme 1.

3.4 *In vitro* release studies

To assess the drug delivery mode of MTX-Mn@PEG in buffers with different pH, an *in vitro* release study was performed. As seen in Fig. 4A, MTX-Mn@PEG exhibited a pH-responsive character for the different release behaviours in pH = 5.5 and 7.4 PBS solutions, which was mainly due to the protonation of the polycarboxylic groups, and the nitrogen heterocycle of MTX in low pH acid conditions then affects the coordination stability of NCPs.[34–36] When MTX-Mn@PEG solution was placed in PBS (pH = 7.4), the release amount accounted for 16.1% after 1.5 h, and after 12 h, reached at a stable stage of 33.2%. When pH = 5.5, a burst-effect was observed within 4 h, releasing 48.9%, and finally being stable at 73.8% after 24 h. This means that MTX-Mn@PEG NCPs are a pH-responsive nanoplatform.

3.5 *In vitro* cytotoxicity evaluation

As a controlled-release antitumor agent, MTX-Mn@PEG would be cytotoxic to cancer cells in a certain time after the release of MTX. Therefore, a cervical cancer cell line (HeLa) was cultivated with different concentrations of MTX and MTX-Mn@PEG for 72 h to evaluate the antitumor capacity of MTX-Mn@PEG (Fig. 4B). The half maximal inhibitory concentration (IC_{50}) value of MTX to HeLa cells (178.4 μg mL^{-1}) was approximated to the value of MTX-Mn@PEG (169.2 μg mL^{-1}). This was reasonable because the antitumor capacity of MTX-Mn@PEG mainly came from MTX after effectively releasing from the NCPs especially in the acidic environment of cancer cells. To confirm that the apoptosis was caused by MTX, the apoptosis of HeLa cells treated with MTX-Mn@PEG for 72 h was evaluated by flow cytometry (Fig. 4C). The percentage of dead cells treated with MTX is 49.9% while that of dead cells treated with MTX-Mn@PEG is 56.0%. These data were in accordance with the MTT assay, further proving that the antitumor capacity of MTX-Mn@PEG mainly came from the released MTX.

3.6 Cell uptake assay

The amount of MTX-Mn@PEG taken up by HeLa cells at different timepoints was measured by flow cytometry and fluorescence (Fig. 5A and C). 10% ICG was successfully loaded into

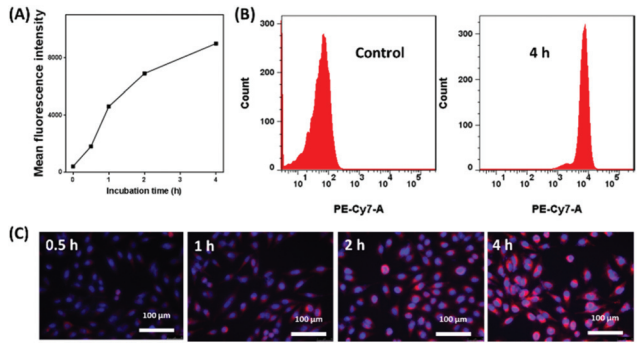

Fig. 5 (A) The semiquantitative intensity of fluorescence emitted from MTX-Mn-ICG@PEG at different time points was analysed by flow cytometry in cells. (B) The flow cytometry histogram results of HeLa cells treated with MTX-Mn-ICG@PEG for 0 h (as a control) and 4 h. (C) Cellular uptake by HeLa cells with fluorescence at different time points; blue fluorescence means that the cellular nucleus is stained with Hoechst 33342, and red fluorescence means that the MTX-Mn-ICG@PEG are uptaken by cells, scale bars: 100 μm.

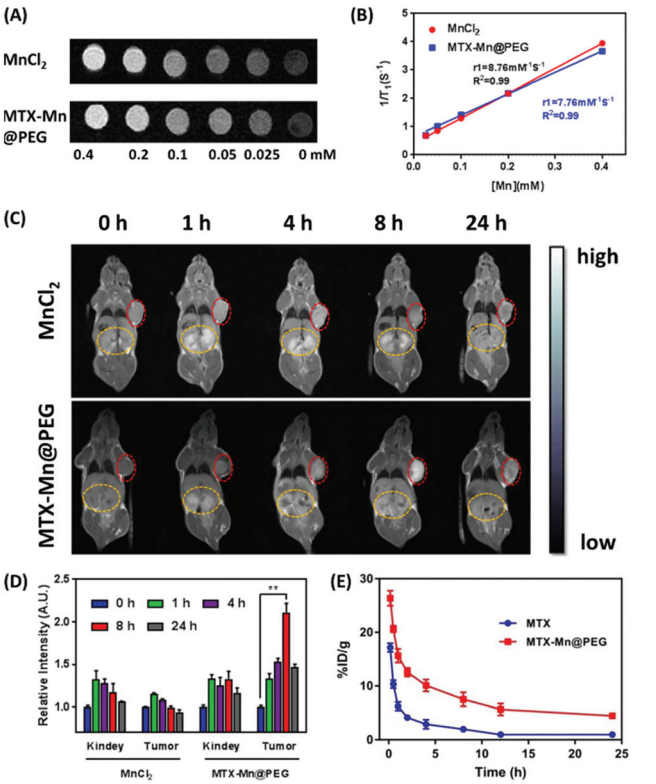

Fig. 6 (A) *In vitro* T_1-weighted MR images of different concentrations of $MnCl_2$ and MTX-Mn@PEG in aqueous solutions. (B) T_1 relaxation rates of $MnCl_2$ and MTX-Mn@PEG. (C) *In vivo* T_1 MR images of $MnCl_2$ and MTX-Mn@PEG at different times post-injection; red circles indicate the tumor and yellow circles indicate the kidneys of the mice. (D) Relative intensity of $MnCl_2$ and MTX-Mn@PEG at the kidney and tumor in (C) (n = 5). (E) The pharmacokinetics of MTX and MTX-Mn@PEG in rat blood circulation detected by HPLC (n = 5), and ** means $P < 0.01$.

the MTX-Mn@PEG (Fig. S3†). The successful loading makes the NCPs emit red fluorescence at 767 nm (PE-Cy7-A channel in a BD FACSCalibur system) for detecting the amount of NCPs in HeLa cells by fluorescence imaging and flow cytometry. The results showed that MTX-Mn@PEG was internalized by HeLa cells after co-culturing for the first 30 minutes. With the increase in the incubation time, more red fluorescence could be observed which indicates that more MTX-Mn@PEG NCPs were uptaken by HeLa cells. Fig. 5B shows that the mean fluorescence intensity of HeLa cells at 0 h is only 172, whereas, after co-culturing with MTX-Mn@PEG for 4 h, the mean fluorescence intensity of the cells increased to 8862 which is nearly 51 fold compared to the cells before treatment.

3.7 *In vitro* and *in vivo* T_1-weighted MR imaging

The *in vitro* longitudinal relaxivity (r_1) of $MnCl_2$ and MTX-Mn@PEG in aqueous solution was measured with the 0.5 T MR scanner. According to the MR images (Fig. 6A), the r_1 value of Mn^{2+} in MTX-Mn@PEG was calculated to be 7.76 M^{-1} S^{-1} (Fig. 6B), which was slightly lower than that of Mn^{2+} in $MnCl_2$ solution. The data suggested that, as an agent of T_1 contrast, the ability of Mn^{2+} in MTX-Mn@PEG was not affected significantly after coordinating into nanoparticles. A pharmacokinetics assay of nanoparticles was performed using the blood of rats to assess the retention time of MTX-Mn@PEG compared to that of MTX (Fig. 6E). The circulation half-lives of MTX in blood were determined to be 0.71 ± 0.15 h, while the half-lives of MTX-Mn@PEG were prolonged to 4.23 ± 1.56 h. *In vivo* T_1-weighted MR images showed that the T_1 signal of $MnCl_2$ enhanced in the kidney and tumor locations very quickly in the first 1 h, and then $MnCl_2$ was cleared by the kidney slowly. After 24 hours, the signal nearly disappeared in the kidney and tumor locations (top lane in Fig. 6C). The T_1 signal of MTX-Mn@PEG was enhanced in the kidney and tumor 1 h after *i.v.* injection, peaked in the tumor at 8 h reaching 2.1 fold compared to that at 0 h, and still remained 1.5 fold after 24 h (bottom lane in Fig. 6C and D), demonstrating its perfect EPR behaviour. All the data implied that MTX-Mn@PEG can extend the circulation time to achieve a better enrichment effect compared with individual MTX and $MnCl_2$.

3.8 *In vivo* antitumor efficacy

The *in vivo* antitumor efficiency of MTX-Mn@PEG compared to that of MTX was investigated by randomly dividing 20 nude mice bearing HeLa tumors into 4 groups when the tumors were about 100 mm^3 (n = 5). The 4 groups were treated with PBS, $MnCl_2$, MTX and MTX-Mn@PEG every 2 or 3 days, respectively. The different growth ratios of tumors in different groups could be found in Fig. 7B–D. The volume of tumors treated with PBS and $MnCl_2$ grew up to 15.7 and 15.9 fold compared to the volume of the PBS group at the beginning day. The volume of the tumors of the MTX group was 7.7 fold compared to that of the PBS group while the volume of tumors treated with MTX-Mn@PEG was 2.6 fold showing the best antitumor efficiency. The antitumor efficiency of MTX-Mn@PEG mainly came from the MTX and EPR effect *in vivo*. The body weight changes during the treatment were used to assess the toxicity of the agents dosed to mice (Fig. 7A). No loss of body

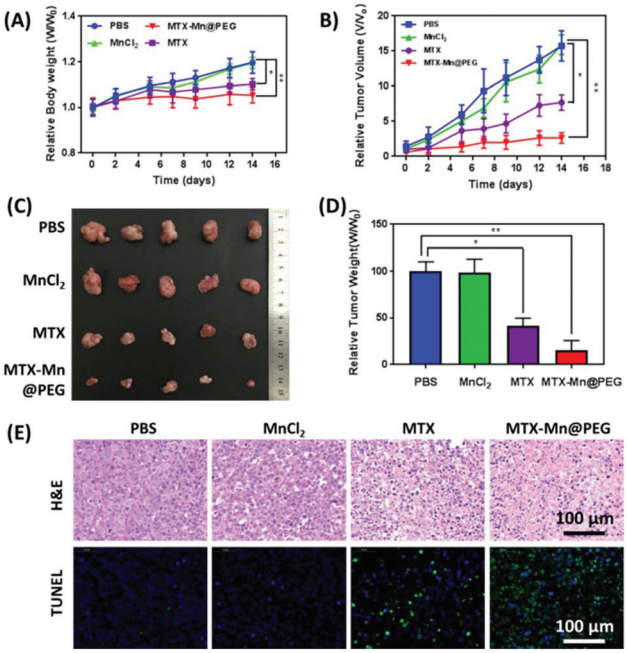

Fig. 7 (A) Relative body weight changes of each group during treatment. (B) Relative tumor volumes of mice during the treatment. (C) Photographs of tumors excised from mice after 14 days' treatment. (D) Relative tumor weight of each group compared to the PBS group. (E) The images of the tumors obtained from mice after treatment, and then staining with H&E and TUNEL; blue fluorescence represents the nucleus, green fluorescence represents terminal deoxynucleotidyl transferase, and * means $P < 0.05$ and ** represents $P < 0.01$, scale bars: 100 μm.

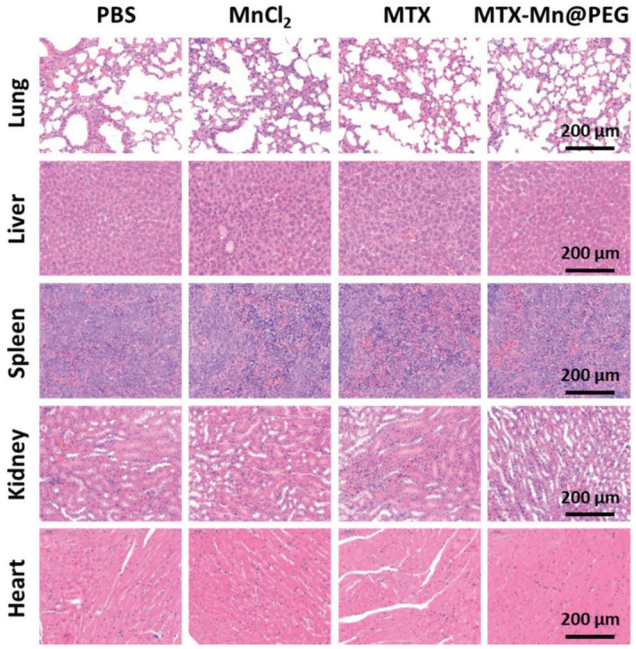

Fig. 8 H&E images of major organs (lung, liver, spleen, kidney and heart) that were extracted from the mice after 14 days' treatment, scale bars: 200 μm.

weight was observed during the treatment, proving the low toxicity to normal tissues of MTX and MTX-Mn@PEG. The increased body weight of PBS and $MnCl_2$ groups was mainly due to the increase of the tumor weight. To further investigate the antitumor efficacy of MTX-Mn@PEG, histological and immunohistochemical analyses of the tumors in different groups were conducted (Fig. 7E). The H&E stained images of groups treated with PBS and $MnCl_2$ showed a uniform and satiation morphology of tumor cells. A lot of fragment areas were observed in MTX and MTX-Mn@PEG groups, indicating that abundant cancer cells were dead. Meanwhile, the TUNEL images, in which the green fluorescence represented the apoptosis of tumor cells, showed similar results to the H&E staining results. From these data, MTX-Mn@PEG NCPs were found to exhibit an excellent antitumor efficiency.

3.9 Histological analysis

The toxicity of $MnCl_2$, MTX and MTX-Mn@PEG was evaluated by H&E staining of the main organs (lung, liver, spleen, kidney and heart) extracted from the mice after 14 days' treatment (Fig. 8). No obvious morphological changes or inflammatory lesions were observed in all major organs, which is consistent with the body weight changes of mice in different groups (Fig. 7A and Fig. S4†). All these results showed that our nanoparticle, MTX-Mn@PEG, exhibited good biocompatibility and high tolerance in mice.

4. Conclusions

In this work, we successfully fabricated simple (chelating agent free), controllable (stoichiometry) and functional (pH-responsive) MTX-Mn@PEG NCPs comprising the drug MTX and MR CA Mn^{2+} *via* coordination and surface coated with a PEG layer. With the PEG on the surface, these NCPs can be stable in blood to enrich in the tumor location *via* the EPR effect. The antitumor efficiency of MTX-Mn@PEG was comparable to that of the free drug MTX *in vitro*, but *in vivo*, its efficiency was enhanced obviously compared with that of the free drug MTX. Additionally, we also realized the diagnosis of cancer by MR imaging with the help of the contrast agent Mn^{2+}. MTX-Mn@PEG NCPs shows several advantages: (1) a chemotherapeutic drug was directly coordinated with MRI CAs replacing the chelating agents, which will reduce the price and the side effect of the MRI based theranostic nanoplatform. (2) We revealed the coordination mechanism of NCPs by the usage of XRD, UV-vis, and FT-IR. (3) The high drug loading capacity, uniform particle size, and a simple synthesis protocol make it easy to produce MTX-Mn@PEG in a large scale. Most of the drugs used in the clinic contain coordination sites and many metal ions show the capability of use as CAs. These novel drug-metal ion based NCPs provide a general theranostic nanoplatform for cancer therapy, and can be expanded to other drugs and bioimaging agent systems.

Conflicts of interest

There are no conflicts to declare.

Acknowledgements

The authors acknowledge the financial support from the National Natural Science Foundation of China (51690151, 21875134 and 21805130), National Key Research and Development Plan of China (Grant No. 2016YFA0201500), Natural Science Foundation of Shanghai (17ZR1441300) and Innovation Fund of Joint Research Center for Precision Medicine in Shanghai Jiao Tong University Affiliated Sixth People's Hospital South Campus (2017B006).

All animal procedures were performed in accordance with the Guidelines for Care and Use of Laboratory Animals of Shanghai Jiao Tong University and approved by the Animal Ethics Committee of Shanghai Jiao Tong University.

References

1 F. Bray, J. Ferlay, I. Soerjomataram, R. L. Siegel, L. A. Torre and A. Jemal, *CA-Cancer J. Clin.*, 2018, **68**, 394–424.
2 J. Ferlay, M. Colombet, I. Soerjomataram, C. Mathers, D. M. Parkin, M. Pineros, A. Znaor and F. Bray, *Int. J. Cancer*, 2019, **144**, 1941–1953.
3 A. Umar, B. K. Dunn and P. Greenwald, *Nat. Rev. Cancer*, 2012, **12**, 835–848.
4 Y. Ma, J. Huang, S. Song, H. Chen and Z. Zhang, *Small*, 2016, **12**, 4936–4954.
5 Q. Chen, H. Ke, Z. Dai and Z. Liu, *Biomaterials*, 2015, **73**, 214–230.
6 H. Huang and J. F. Lovell, *Adv. Funct. Mater.*, 2017, **27**, 1603524.
7 S. St-Jean, P. Coupe and M. Descoteaux, *Med. Image Anal.*, 2016, **32**, 115–130.
8 Z. Gao, T. Ma, E. Zhao, D. Docter, W. Yang, R. H. Stauber and M. Gao, *Small*, 2016, **12**, 556–576.
9 P. R. Shaha, R. Khetawat, K. Sahoo, A. Garg, M. A. Ilyas, G. Khairnar, S. Garg and S. H. Budgemwar, *J. Clin. Diagn. Res.*, 2017, **11**, TC01–TC05.
10 B. H. McDonagh, G. Singh, S. Hak, S. Bandyopadhyay, I. L. Augestad, D. Peddis, I. Sandvig, A. Sandvig and W. R. Glomm, *Small*, 2016, **12**, 301–306.
11 Y. D. Xiao, R. Paudel, J. Liu, C. Ma, Z. S. Zhang and S. K. Zhou, *Int. J. Mol. Med.*, 2016, **38**, 1319–1326.
12 M. L. Belyanin, E. V. Stepanova, R. R. Valiev, V. D. Filimonov, V. Y. Usov, O. Y. Borodin and H. Ågren, *Chem. Phys. Lett.*, 2016, **665**, 111–116.
13 Z. C. Liao, C. R. Li and Z. Y. Yang, *Synth. React. Inorg., Met.-Org., Nano-Met. Chem.*, 2015, **46**, 653–658.
14 X. Wang, L. Xu, Z. Ren, M. Fan, J. Zhang, H. Qi and M. Xu, *Colloids Surf., B*, 2019, **183**, 110452.
15 L. T. Shen, H. Y. Zhao, J. Du and F. Wang, *In Vivo*, 2005, **19**, 233–236.
16 M. Rogosnitzky and S. Branch, *BioMetals*, 2016, **29**, 365–376.
17 J. L. Vivero-Escoto, R. C. Huxford-Phillips and W. B. Lin, *Chem. Soc. Rev.*, 2012, **41**, 2673–2685.
18 J. Liu, Q. Chen, W. Zhu, X. Yi, Y. Yang, Z. Dong and Z. Liu, *Adv. Funct. Mater.*, 2017, **27**, 1605926.
19 Y. Yang, J. Liu, C. Liang, L. Feng, T. Fu, Z. Dong, Y. Chao, Y. Li, G. Lu, M. Chen and Z. Liu, *ACS Nano*, 2016, **10**, 2774–2781.
20 D. Liu, C. Poon, K. Lu, C. He and W. B. Lin, *Nat. Commun.*, 2014, **5**, 4182.
21 W. J. Rieter, K. M. Pott, K. M. L. Taylor and W. B. Lin, *J. Am. Chem. Soc.*, 2008, **130**, 11584–11585.
22 R. Xing, Q. Zou, C. Yuan, L. Zhao, R. Chang and X. Yan, *Adv. Mater.*, 2019, **31**, e1900822.
23 M. Hou, Y. E. Gao, X. Shi, S. Bai, X. Ma, B. Li, B. Xiao, P. Xue, Y. Kang and Z. Xu, *Acta Biomater.*, 2018, **77**, 228–239.
24 Y. Zhao, Y. Guo, R. Li, T. Wang, M. Han, C. Zhu and X. Wang, *Sci. Rep.*, 2016, **6**, 28983.
25 M. Botta, F. Carniato, D. Esteban-G, C. Platas-Iglesias and L. Tei, *Future Med. Chem.*, 2019, **11**, 1461–1483.
26 N. Rastogi, N. Tyagi, O. Singh, B. S. Hemanth Kumar, U. P. Singh, K. Ghosh and R. Roy, *J. Inorg. Biochem.*, 2017, **177**, 76–81.
27 H. Zhou, Z. Fan, P. Y. Li, J. Deng, D. C. Arhontoulis, C. Y. Li, W. B. Bowne and H. Cheng, *ACS Nano*, 2018, **12**, 10130–10141.
28 J. Pan, X. Zhu, X. Chen, Y. Zhao and J. Liu, *Biomater. Sci.*, 2018, **6**, 372–387.
29 E. Li, X. Cheng, Y. Deng, J. Zhu, X. Xu, P. E. Saw, H. Gu, C. Ge and Y. Pan, *Biomater. Sci.*, 2018, **6**, 1892–1898.
30 D. M. Liu, S. A. Kramer, R. C. Huxford-Phillips, S. Z. Wang, J. D. Rocca and W. B. Lin, *Chem. Commun.*, 2012, **48**, 2668.
31 C. Zhang, Y. Che, Z. Zhang, X. Yang and L. Zang, *Chem. Commun.*, 2011, **47**, 2336–2338.
32 X. F. Zhao, Z. L. Liu, X. D. Li, S. P. Li and F. G. Song, *J. Phys. Chem. Solids*, 2019, **124**, 73–80.
33 Y. Wang, X. Yang, J. Yang, Y. Wang, R. Chen, J. Wu, Y. Liu and N. Zhang, *Carbohydr. Polym.*, 2011, **86**, 1665–1670.
34 H. Zheng, L. Xing, Y. Cao and S. Che, *Coord. Chem. Rev.*, 2013, **257**, 1933–1944.
35 S. Li, Q. Zou, Y. Li, C. Yuan, R. Xing and X. Yan, *J. Am. Chem. Soc.*, 2018, **140**, 10794–10802.
36 Y. Li, Q. Zou, C. Yuan, S. Li, R. Xing and X. Yan, *Angew. Chem., Int. Ed.*, 2018, **57**, 17084–17088.